ADVANCED MATERIALS TECHNOLOGIES
www.advmattechnol.de

A Flexible Flow Velocity Sensor Based on Core-Sheath Structured Triboelectric Nanogenerator for Underwater Environmental Monitoring

Haoyang Song, Shuai Zhang, Hengxu Du, Cong Zhao, Jicang Si, Mengwei Wu,* and Minyi Xu**

Traditional flow velocity sensors have limitations such as limited accuracy, environmental interference, and dependence on power supply. The high-precision measurement and stable output of the flow velocity sensor are of great significance for the accuracy and reliability of marine environmental monitoring. The triboelectric nanogenerator (TENG), an emerging technology for energy harvesting and sensing, offers a promising solution for real-time flow velocity monitoring. This paper presents a core-sheath structured triboelectric nanogenerator (CS-TENG) with an innovative design featuring flexible materials to enhance environmental adaptability. By leveraging the vortex-induced vibration (VIV) effect, the device achieves efficient fluid kinetic energy harvesting through VIV-induced mechanical vibration coupling, enabling omnidirectional flow velocity measurement. The experimental results show that the frequency of the output signal from CS-TENG has a good linear relationship with the flow velocity, specifically, within a flow velocity range of 0.297–0.931 m s^{-1}, the correlation coefficient reached to 0.992. Wireless real-time flow velocity monitoring is achieved by integrating the MCU with the LoRa. The results show that the CS-TENG, as a high-precision active sensor, provides an intelligent solution for marine environmental monitoring.

1. Introduction

As the exploitation of marine resources and the development of offshore platforms grow, real-time monitoring of the marine environment has become increasingly essential.[1,2] Underwater structures, including mooring lines, rises, and pipelines, are vulnerable to vortex-induced vibration (VIV) effect caused by ocean current.[3–5] These vibrations can accelerate fatigue damage and may ultimately lead to structural failure. Therefore, real-time monitoring of flow velocity and flow direction is crucial for ensuring the safety and extending the service life of offshore platforms.[6,7]

Currently, mechanical, electromagnetic, and acoustic ocean flow meters are commonly used to measure flow velocity. Mechanical flow meters measure velocity by detecting the rotational speed of rotating element.[8] While this type of flow meter is not restricted by depth, it has limited accuracy at low flow velocities and is prone to wear and corrosion of mechanical moving parts. Electromagnetic flow meters utilize Faraday's principle of electromagnetic induction to measure flow velocity by detecting the induced electric potential as seawater flows through a magnetic field.[9] However, this method is susceptible to interference from ambient magnetic fields, and the measurements are significantly influenced by the conductivity of seawater.[10,11] Acoustic flow meters rely on the Doppler shift phenomenon to calculate flow velocity by measuring the time difference or frequency change between transmitted and received acoustic signals.[12] While they offer high accuracy, these meters are expensive, complex, which restrict their use in complex marine environments.

In contrast, vortex flow meters estimate flow velocity by measuring the frequency of vortex shedding. This type of meter is simple in design, cost-effective, low-maintenance, and highly stable.[13–15] However, most existing vortex flow meters rely on front blunt bodies to generate vortex shedding, which leads to complex installation and arrangement as well as restrictions on flow directions. Additionally, the positioning of the components within vortex flow meters that are sensitive to vortex shedding must be adjusted according to the flow velocity range. This limitation reduces their effectiveness in open ocean environments. Moreover, these sensors belong to passive sensors, and passive sensors have a high dependence on power supplies, making deployment in remote and deep-sea environments difficult.

The concept of triboelectric nanogenerator (TENG) put forward by Zhonglin Wang in 2012, which can function as an

H. Song, S. Zhang, H. Du, J. Si, M. Wu, M. Xu
Dalian Key Lab of Marine Micro/Nano Energy and Self-Powered Systems
Marine Engineering College
Dalian Maritime University
Dalian 116026, China
E-mail: sjc@dlmu.edu.cn; wumengwei@dlmu.edu.cn; xuminyi@dlmu.edu.cn
C. Zhao
Navigation and Ship Engineering
Dalian Ocean University
Dalian 116023, China

The ORCID identification number(s) for the author(s) of this article can be found under https://doi.org/10.1002/admt.202500704

DOI: 10.1002/admt.202500704

active sensor, provides a novel way for the development of large-scale real-time monitoring networks.[16,17] These sensors that do not rely on an additional power supply. They can capture energy from the ocean environment, such as wind, waves, and currents, and then convert it into electrical energy. In this way, they can function without external power supply, which is different from passive sensors.[18–20] TENG, as an emerging sensing technology, vias the phenomena of triboelectric effect and electrostatic induction to realize energy conversion.[21–26] It possesses advantages such as no need for an external power supply, high sensitivity, rapid response time, and easy miniaturization, providing a new strategy to realize real-time monitoring of flow velocity.[27–32]

In recent years, TENGs have made significant advancements in natural environment monitoring, including applications in wind speed and water flow measurement.[33–35] Deng et al. designed a flow velocity sensor based on TENG that utilizes the VIV effect.[36] This sensor uses cylindrical motion to drive the contact-separation between bottom dielectric materials (FEP and Cu), and measures flow velocity based on the relationship between electric charge and flow velocity. Cheng et al. developed a fully enclosed spherical flow velocity sensor based on the contact separation mode of TENG.[37] The sensor uses the rotation of paddles to drive the internal rotation of the sphere, generating an electrical signal. Wang et al. developed a rotating disk-type flow velocity sensor based on the independent layer mode of TENG.[38] The sensor uses the turbine's rotation to drive relative motion between the stator (Nylon) and rotor (PVC), generating an electrostatic sensing phenomenon through cyclic rotation. Zhang et al. designed a triple-cylinder flow velocity sensor based on the contact-separation mode of TENG.[39] Driven by a gear system with triboelectric contact separation between materials (Ni and silicone), the sensor calculates real-time flow velocity. He designed a TENG-based flow velocity sensor for non-full pipe fluid monitoring, which utilizes a water wheel to drive flexible blades (FEP) to slide between copper electrodes, generating electrical signals.[40]

The flow velocity sensors-based TENGs also face multiple limitations. In underwater conditions, humidity reduces the charge density and electron transfer efficiency of triboelectric materials, decreasing the output amplitudes of TENG.[41,42] So many of these sensors determine flow velocity by correlating the frequency of electrical signal with the flow velocity. However, some have a high minimum flow velocity threshold (e.g., 2 m s^{-1}), making them unsuitable for most marine environments with lower flow velocity. Sensors with rotational designs encounter issues like slow response and dielectric materials wear.[43,44] Additionally, certain sensors, such as those relying on water-driven gear rotation, are mainly applicable in near-shore or riverine environments. Meanwhile, sensors based on TENGs urgently need to address issues such as high-frequency response and gravity sensitivity.[45] In light of the above-mentioned limitations, there is an urgent need to find a novel and efficient sensor design that can overcome these obstacles, achieve high-precision flow velocity measurement.

In this paper, a flexible core-sheath structured triboelectric nanogenerator (CS-TENG) based on the VIV effect is proposed. Due to its innovative flexible core-sheath design, this flow velocity sensor not only overcomes the limitations of the front blunt body design but also maintains advantages like fast response, low start-up flow velocity. First, this paper presents a theoretical model that integrates both mechanical and electrical aspects. Then, numerical simulations are conducted to validate the model's accuracy. Subsequently, the effects of the CS-TENG's structural parameters on its performance are analyzed in detail. The performance of the optimized CS-TENG is experimentally evaluated. The experimental results demonstrate a strong linear correlation (R^2 = 0.992) between the frequency of the output signal and flow velocity, within the range of 0.297–0.931 m s^{-1}. Its fully enclosed structure effectively reduces the effects of seawater salinity, conductivity, and humidity on measurement accuracy. Additionally, by adjusting the structural parameters of the CS-TENG, such as the type of Silicone used in the outer sheath, the frequency-flow velocity relationship can be optimized to suit different flow velocity environments. Finally, this paper also demonstrates its application value and broad prospect in marine environment monitoring.

2. Result and Discussion

2.1. Structure and Working Principle of CS-TENG

The CS-TENG offers versatile applications in marine environmental monitoring, particularly for real-time ocean current tracking around offshore platforms, as shown in **Figure 1**a. This capability provides critical data for comprehensive marine environmental assessments in such dynamic ecosystems. Its functionality relies on a vortex-induced vibration (VIV) response mechanism: the outer sheath undergoes lateral vibrations perpendicular to the incoming flow due to VIV effect, triggering contact-separation motion between the outer sheath and inner core, as illustrated in Figure 1b. Structurally, the CS-TENG features a dual-component design-an outer sheath and inner core—both constructed from flexible materials to enhance sensitivity and adaptability, as depicted in Figure 1c. This flexibility enables the outer sheath to vibrate robustly in response to flow excitation, while the inner core accommodates sheath movement to ensure stable contact-separation and efficient charge generation.

The manufacturing process employs a secondary infusion technique to embed conductive yarns within a silicone outer sheath and wraps a metal wire around a silicone rod for the inner core, as shown in Figure S1 (Supporting Information). This design establishes silicone as the negative triboelectric material (outer sheath) and metal wire as both the positive triboelectric material and electrode (inner core). During contact-separation, electronegativity differences between materials generate an external current, converting fluid kinetic energy into electrical energy. The sensor achieves high-precision flow velocity monitoring through a direct correlation between output signal frequency and flow velocity (validated in subsequent experiments). A physical diagram of the device, shown in Figure S2 (Supporting Information), illustrates its fully enclosed structure, which mitigates ambient humidity interference, and the durable silicone outer sheath. These features, combined with its compact size and simple fabrication, underscore the CS-TENG's practical utility.

When delving into the transverse vibration characteristics of the structure, assuming the transverse displacement of the structural cross-section depends on both time and spatial coordinates $Y(Z,T)$, the equation governing the transverse vibration

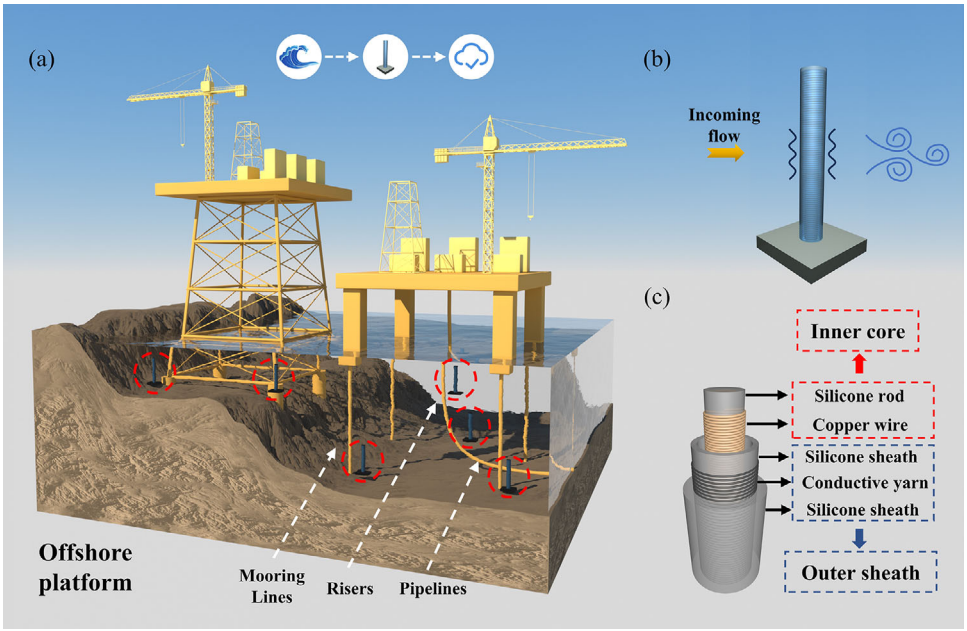

Figure 1. a) Potential application scenario of CS-TENG for environmental monitoring. b) Response mechanism of CS-TENG to the excitation of incoming flow. c) Structural design of CS-TENG includes inner core and outer sheath.

of the structure-considering the effects of tension and flexural stiffness—is given by:[46]

$$m\frac{\partial^2 Y}{\partial T^2} + c\frac{\partial Y}{\partial T} + EI\frac{\partial^4 Y}{\partial Z^4} - T_e\frac{\partial^2 Y}{\partial Z^2} = F_y \tag{1}$$

Here, m is the structural mass, c is the structural damping, E is the modulus of elasticity of the structure, I is the moment of inertia of the structure, EI is the flexural rigidity of the structure, T_e is the tension per unit length of the structure, and F_y is the total force exerted on the structure in the transverse direction.

Based on the understanding of structural transverse vibration and its governing equation, when the structure is excited by a uniform incoming flow with velocity U, it undergoes a lift force F_L perpendicular to the flow direction and a drag force F_D parallel to the flow direction. For small angle of attack α, these forces induce structural deflection, where the deflection angle corresponds to the angle of attack, as shown in **Figure 2a**.

$$\begin{cases} \sin\alpha = \dfrac{-\partial Y/\partial T}{\sqrt{U^2+(\partial Y/\partial T)^2}} \approx \dfrac{-\partial Y/\partial T}{U} \\ \cos\alpha = \dfrac{U}{\sqrt{U^2+(\partial Y/\partial T)^2}} \approx 1 \end{cases} \tag{2}$$

At this point, the total force F_y acting on the structure in the lateral direction is:

$$F_y = F_L\cos\alpha + F_D\sin\alpha \tag{3}$$

Here, the lift force F_L is composed of the potential force F_p and the vortex lift force F_v:[47]

$$F_p\cos\alpha = -C_A\frac{\pi D^2\rho}{4}\frac{\partial^2 Y}{\partial T^2} \tag{4}$$

$$F_v = C_v\frac{\rho D}{2}U^2 \tag{5}$$

$$F_D = C_D\frac{\rho D}{2}U^2 \tag{6}$$

Here, C_A, C_V, and C_D represent the potential force coefficient, vortex lift force coefficient, and drag force coefficient, respectively. Additionally, D represents the structure's diameter, ρ is the fluid density.[48]

Considering the governing equation of the structure's transverse vibration in Equation (1) and the expressions of the forces along with the relevant coefficients in Equation (4), Equation (5), and Equation (6), substituting the latter into the former yields the transverse vibration equation of the structure. Following the substitution, the formula for the transverse vibration equation is presented below:

$$\left(m + C_A\frac{\pi D^2\rho}{4}\right)\frac{\partial^2 Y}{\partial T^2} + \left(c + \frac{C_D\rho DU}{2}\right)\frac{\partial Y}{\partial T} + EI\frac{\partial^4 Y}{\partial Z^4} - T_e\frac{\partial^2 Y}{\partial Z^2} = C_v\frac{\rho DU^2}{2} \tag{7}$$

From Equation (7), the kinematic state of the CS-TENG is significantly influenced by multiple key factors, including the sheath diameter, the structural bending stiffness, and the incoming flow velocity.

COMSOL Multiphysics simulations were conducted to analyze the dynamic response of the CS-TENG to incoming flow excitation. Results show that the perpendicular displacement of the sheath correlates with flow velocity. Grid independence verification is provided in Figure S3a (Supporting Information). With

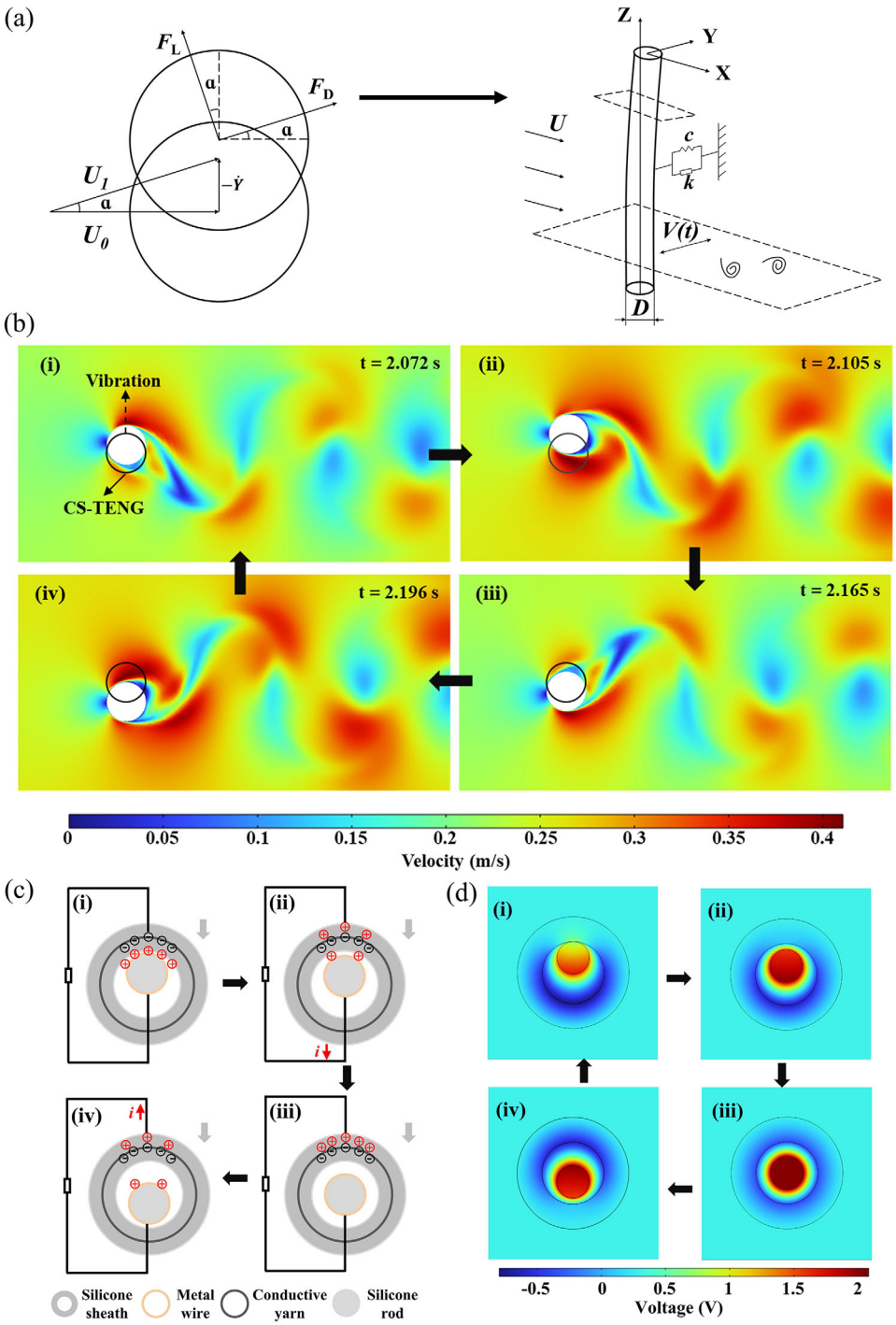

Figure 2. a) Schematic diagram of mechanical model analysis process. b) Numerical simulation of the kinematic state of the axial section by COMSOL Multiphysics at different time. c) Electron transfer process of CS-TENG. d) Numerical simulation of the potential distribution by COMSOL Multiphysics during the working process.

an incoming flow velocity set to 0.25 m s^{-1}, the corresponding numerical simulation results are presented in Figure 2b.

As water flows over the surface of the outer sheath, a low-velocity zone forms in front of the outer sheath. The water then moves along the upper and lower sides of the sheath, creating a high-velocity zone. The periodic shedding from the upper and lower sides of the flow separation induces vortex street formation on the right side of the outer sheath, leading to the alternative existence of high-pressure and low-pressure zones on its outer surface. This pressure difference between the upper and lower sides generates a lifting force on the outer sheath surface, as illustrated in Figure S3d (Supporting Information), causing periodic

vibration under the excitation of water flow. This vibration results in a periodic contact-separation phenomenon between the outer sheath and the inner core.

During t = 2.072 s to t = 2.105 s, the high-velocity zone on the upper side and low-velocity zone on the lower side of the outer sheath produce an upward lifting force, causing the outer sheath to vibrate upward (as shown in Figure 2b i,ii). Conversely, when the high- and low-velocity zones switch positions between t = 2.165 s and t = 2.196 s, a downward lifting force is generated, leading to downward vibrations (as shown in Figure 2b iii,iv). For a flow velocity of 0.25 m s^{-1}, the lift force profile on the sheath and its displacement perpendicular to the incoming flow direction are depicted in Figure S3b,c (Supporting Information).

The CS-TENG operates in the contact-separation mode, with its electron transfer process divided into four distinct stages, As shown in Figure 2c,i) The outer sheath oscillates to one side due to the VIV effect (as shown to the up), bringing it into contact with the inner core. Due to triboelectric effect and the electronegativity difference between the silicone and metal wire, equal positive and negative charges are distributed on the surfaces of both, reaching electrostatic equilibrium. ii) As the outer sheath vibrates to the down, the contact between the outer sheath and inner core is broken, disrupting the electrostatic equilibrium. This causes free electrons to flow from the metal wire to the conductive yarn through electrostatic induction. This electron flow balances the potential difference, generates an electric potential, and finally forms an electric current. iii) As the outer sheath continues to move downward, it completely separates from the inner core, restoring the electrostatic equilibrium. iv) As the sheath oscillates further, the electrostatic equilibrium is broken once again, causing the free electrons to flow in the reverse direction, generating a reverse current. Based on the above electron transfer process, the CS-TENG converts the external excitation into its own vibrations, which then generate an electrical signal.

The potential difference between the two electrodes of a contact-separated TENG is given by the following equation:[49]

$$V = E_1 d_1 + E_2 d_2 + E_{air} y(t) \tag{8}$$

Here, E_1, E_2, and E_{air} are the internal electric field strengths of the two triboelectric materials and the air, d_1 and d_2 are the thicknesses of the triboelectric materials, $y(t)$ is the distance between them. It should be noted that in the structure proposed in this paper, the copper wire is used as both the positive triboelectric material and the electrode, so its thickness can be neglected and thus $d_1 = 0$ mm.

The *V-Q-x* theoretical model, which represents the output performance of the CS-TENG, is derived by calculating the electric field strength using Gauss' theorem and substituting the result into Equation (8).

$$V = E_2 d_2 + E_{air} x = -\frac{Q}{S\epsilon_0}\left[\frac{d_2}{\epsilon_{r2}} + y(t)\right] + \frac{\sigma y(t)}{\epsilon_0} \tag{9}$$

Here, Q is the transferred charge, σ is the surface charge density of the triboelectric material, ϵ_0 and ϵ_{r2} are the vacuum dielectric constant and the relative dielectric constant of the electronegative triboelectric material, S is contact area between triboelectric materials.

From Equation (9), the output performance of the CS-TENG is prominently influenced by multiple crucial factors, including the type and thickness of the triboelectric materials and the spacing between them.

Numerical simulations were carried out using COMSOL Multiphysics to analyze the potential distribution of the outer sheath and inner core at various positions, as shown in Figure 2d. As expected, the potential difference on the contact surfaces of the outer sheath and inner core varied during the contact-separation process, confirming the validity of the electron transfer mechanism.

By choosing appropriate triboelectric materials and optimizing the structural parameters, the motion dynamics and output performance of the CS-TENG can be enhanced, thereby improving its sensing capabilities.

2.2. The Output and Characteristics of CS-TENG

In this study, the experimental setup consists of a circulating flume that generates water flow and relevant devices that collect electrical signals. The detailed descriptions of these devices will be presented in the Experimental Section. As shown in **Figure 3**a, to clearly present the structural parameters of the CS-TENG, its outer sheath length (L) is specified as 6 cm, and the inner core diameter (d) and outer sheath diameter (D) are labeled. These parameters will be further discussed and analyzed in subsequent sections to clarify their impacts on the performance of the sensor.

The signal-to-noise ratio, an important indicator for evaluating sensor performance, is calculated as the ratio between the output signal of the sensor and the noise signal generated by the sensor itself.

$$SNR = 201\mathrm{g}\,\frac{V_{signal}}{V_{noise}} \tag{10}$$

The voltage signal of the CS-TENG is the focus of further study. At a flow velocity of 0.557 m s^{-1}, the average amplitudes of its voltage, current, and transferred charge signals were measured as 1.33 V, 138.06 pA, and 0.13 nC respectively, while the noise signals under stationary conditions were 0.01 V, 3.48 pA, and 0.01 nC. As a result, the corresponding signal-to-noise ratios were 42.33, 31.96, and 21.11 dB, as shown in Figure 3b. Given these results, the voltage signal shows the highest signal-to-noise ratio, making it more suitable for sensing applications.

Experiments were conducted to investigate the factors influencing the output performance and kinematic state of the CS-TENG. Based on these findings, the most effective triboelectric materials and structures were selected to optimize the sensing performance of the CS-TENG.

The selection of copper wire as the material for the inner core is based on its superior performance. When different materials (Ag, Al, and Cu) served as the positive triboelectric layer with Ecoflex00-20 silicone material as the negative triboelectric layer, as presented in Figure S4a (Supporting Information), the combination of copper wire and Ecoflex00-20 silicone material achieved the highest output performance, with a peak voltage of 1.34 V. Moreover, as shown in Figure S4b (Supporting Information), the voltage signals after Fast Fourier Transform processing indicated

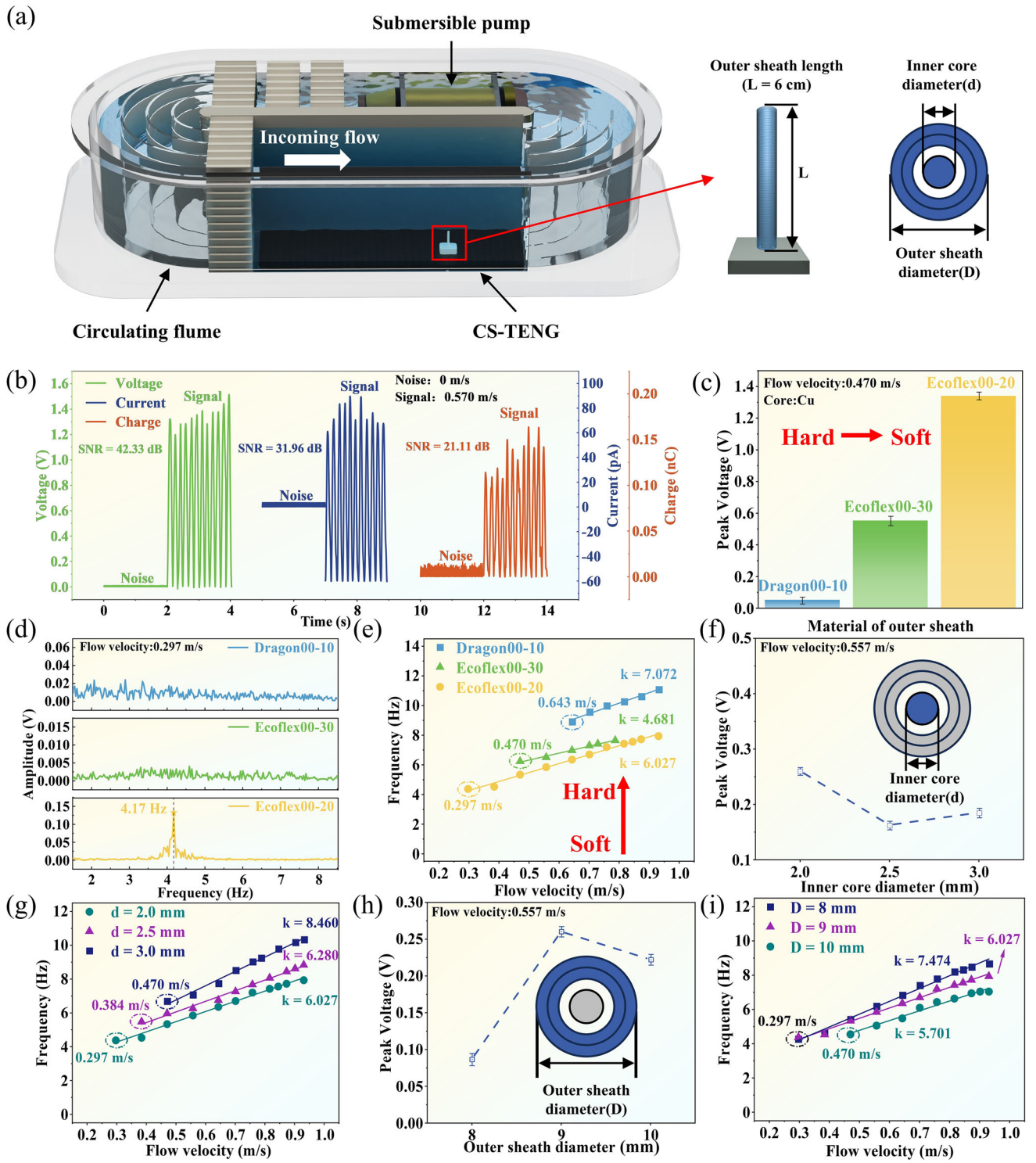

Figure 3. a) Diagram of the Experimental System: Circulating Flume and Dimensions of CS - TENG Components. b) Signal-to-noise ratios at 0 and 0.570 m s^{-1}. c) Peak voltage of different outer sheath materials at 0.470 m s^{-1}. d) Amplitude plots of the output signals of different outer sheath materials at 0.297 m s^{-1}. e) Flow velocity-frequency relationship of different outer sheath materials. f) Peak voltage of different the inner core diameters at 0.557 m s^{-1}. g) Flow velocity-frequency relationship of different the inner core diameters. h) Peak voltage of different the outer sheath diameters at 0.557 m s^{-1}. i) Flow velocity-frequency relationship of different outer sheath diameters.

that the amplitude plot for the copper wire as the positive triboelectric layer was clearer.

The selection of Ecoflex00-20 silicone material as the outer sheath is based on its superior performance. When different silicone materials (Dragon00-10, Ecoflex00-30, Ecoflex00-20) were used as the negative triboelectric layer with copper wire as the positive triboelectric layer, Figure 3c shows that Ecoflex00-20 silicone material provided the best output performance. Under the excitation of incoming flow (0.297 m s^{-1}), Figure 3d presents the output voltage signal amplitude plots of the three sensors with different silicone materials. It is evident that the sensor using Ecoflex00-20 as the outer sheath material has a distinct main frequency, while the other two sensors do not show a clear main frequency. This indicates that when the outer sheath is made of Ecoflex00-20 silicone material, the start-up flow velocity is the lowest, which is attributed to the high flexibility of Ecoflex00-20 with a Shore hardness of only 00-20, enabling it to respond to smaller external excitations. Figure 3e shows the flow velocity-frequency relationship of the CS-TENG for different silicone materials, with the values of the coefficient of determination R^2 being 0.978, 0.990, 0.991 from top to bottom. Based on the initiation flow velocity and the linear fit of the flow velocity-frequency data, Ecoflex00-20 silicone was chosen as the outer sheath material.

The optimal inner core diameter of 2.0 mm is selected based on peak voltage and start-up velocity performance. As shown in Figure 3f, the highest peak voltage of 0.26 V is achieved with an inner core diameter of 2 mm, which aligns with Equation (9): a larger distance between triboelectric materials during separation generates a greater potential difference. For diameters of 2.5 and 3.0 mm, peak voltages are lower due to competing effects of distance $y(t)$ and contact area S: smaller contact area reduces charge transfer. When the inner core diameter is 2.5 mm, the reduction in the distance between the triboelectric materials leads to a relatively rapid decrease in the potential difference term in Equation (9), overpowering the increase in charge transfer caused by the slightly larger contact area. Thus, the distance has a greater impact on the output performance. Conversely, when the inner core diameter is 3.0 mm, although the distance continues to decrease, the substantial increase in the contact area starts to have a more dominant influence on the total transferred charge Q. As a result, the contact area S becomes the more significant factor affecting the peak voltage. Figure 3g further shows the flow velocity-frequency relationship for different inner core diameters, with coefficient of determination R^2 values of 0.988, 0.990, and 0.991 from top to bottom. Notably, the 2.0 mm diameter yields the lowest start-up flow velocity of 0.297 m s^{-1}.

The optimal outer sheath diameter of 9 mm is selected based on peak voltage and start-up flow velocity performance. As shown in Figure 3h, the highest peak voltage of 0.26 V is obtained at an outer sheath diameter of 9 mm. In contrast, a peak voltage of only 0.08 V is observed at 8 mm. This discrepancy can be well explained by Equation (9). At an outer sheath diameter of 8 mm, the relatively thin wall (1 mm) allows some electrons to escape through the conductive yarn. The transferred charge Q is a key factor influencing the output voltage. A reduction in transferred charge leads to a decrease in the output voltage. For a diameter of 10 mm, the peak voltage is slightly lower than at 9 mm. From the perspective of Equation (7), the thicker outer wall increases the structural mass m and changes the moment of inertia of the structure I. This results in a smaller oscillation amplitude as the structure becomes more resistant to vibration. Referring back to Equation (9), the reduced oscillation amplitude causes insufficient contact between triboelectric materials, decreasing the contact area S. A smaller contact area reduces the transferred charge, which in turn lowers the output voltage. Figure 3i further presents the flow velocity-frequency relationship for different outer sheath diameters, with coefficient of determination R^2 values of 0.991, 0.991, and 0.979 from top to bottom. The slope k differences in the fitting can be explained by Equation (7): larger outer sheath diameters increase structural mass m and moment of inertia I, enhancing inertia and reducing vibration acceleration under the same fluid force. This results in decreased slope values (k = 7.474 for 8 mm, 6.027 for 9 mm, 5.701 for 10 mm), confirming that higher mass and moment of inertia weaken frequency sensitivity to flow velocity as predicted by the equation. Notably, outer sheath diameters of 8 mm and 9 mm exhibit a start-up velocity of 0.297 m s^{-1}, whereas a diameter of 10 mm results in a higher start-up flow velocity of 0.470 m s^{-1}.

The sensing performance of CS-TENG was next tested in the experiment using the preferred triboelectric material and structural parameters. At lower flow velocities, the V_{oc} (open-circuit voltage) of CS-TENG increases with flow velocity, but a decrease is observed at 0.643 m s^{-1}, as shown in **Figure** 4a. This phenomenon can be attributed to the following: as the flow velocity further increases, the contact-separation frequency between the inner core and the outer sheath increases accordingly. During this process, the relative motion state between the inner core and the outer sheath changes. At higher flow velocities, the inner core restricts the movement of the outer sheath, causing the outer sheath and the inner core to remain in continuous contact on the right side (the "right side" here is the incoming flow direction). This reduces the effective contact-separation area between them, reducing the amount of charge transfer and thus the open-circuit voltage V_{oc}. As the flow velocity increases from 0.297 to 0.643 m s^{-1}, the frequency of the V_{oc} signal rises from 4.17 to 6.22 Hz, as shown in Figure 4b. The maximum voltage in Figure 4a reflects transient mechanical excitation, while the peak amplitude in Figure 4b corresponds to the sensor's resonant frequency at steady-state, vortex-induced vibration. Within the 0.297–0.931 m s^{-1} range, the experimentally obtained main frequency of the output electrical signal exhibits a strong linear correlation with flow velocity, as shown in Figure 4c, described by the fitting equation $y = 6.027x + 2.46727 (R^2 = 0.992)$.

The CS-TENG maintains stable electrical signal output across different arrangement angles, which was examined by positioning the sensor perpendicular to the incoming flow direction and varying the angle β between the sensor and the ground, as shown in Figure S5a (Supporting Information). Figure 4d illustrates the main frequency of the CS-TENG output electrical signals at different arrangement angles, with excitation from a 0.557 m s^{-1} incoming flow.

The CS-TENG exhibits a rapid response time of 1.062 s as a flow velocity sensor: When the submersible pump was activated, the CS-TENG began oscillating, but initially, the oscillation was unstable, and the output was low. After 1.062 s, the oscillation stabilized, and the output reached its peak value at that flow velocity, as shown in Figure 4e. This remarkable response

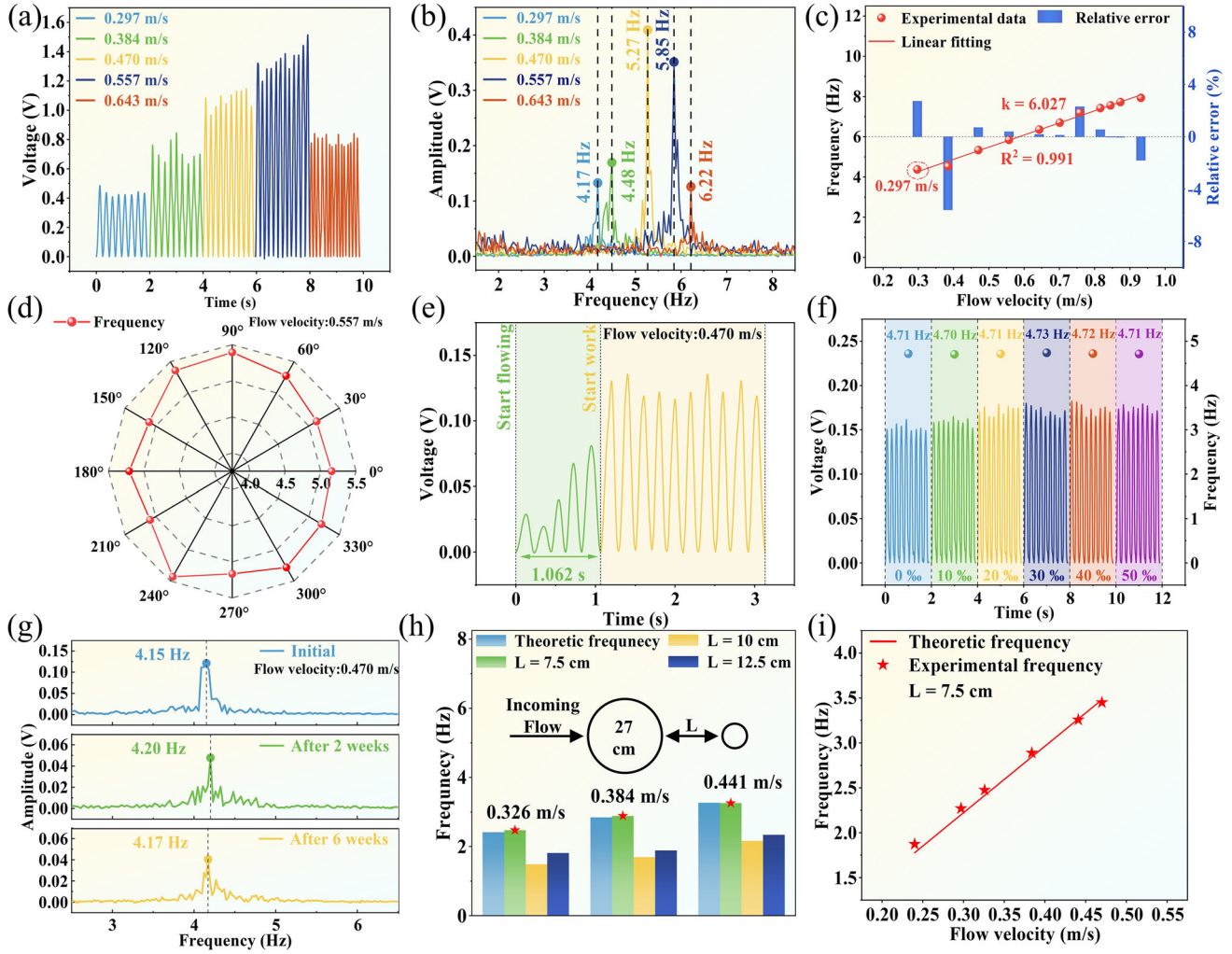

Figure 4. a) V_{oc} at different flow velocities. b) The amplitude plots at different flow velocities. c) Flow velocity-frequency relationship from 0.297 to 0.931 m s^{-1}. d) Frequency of voltage signals at different arrangement angles. e) Response time of CS-TENG after start flowing. f) The V_{oc} and the corresponding frequency under different salinity environments. g) Durability test result of the CS-TENG within 6 weeks. h) Comparison of the theoretical frequency and the main frequency at different distances with a blunt body. i) Relationship between flow velocity and frequency with a blunt body from 0.297 to 0.470 m s^{-1}.

speed is attributed to the sensor's unique flexible core-sheath design, which allows it to quickly adapt to the excitation in flow and reach a stable state. The CS-TENG demonstrated stable output performance across different salinity conditions ranging from 0% to 50 ‰, indicating its high environmental stability. At a flow velocity of 0.557 m s^{-1}, both V_{oc} and the corresponding electrical signal's main frequency remain stable at 4.71 Hz as shown in Figure 4f, demonstrating its feasibility for marine environments. For durability assessment, under 0.384 m s^{-1} flow excitation, the voltage signal's main frequency is 4.15 Hz as shown in Figure 4g. After two weeks and six weeks of immersion in water, the amplitude of the main frequency decreases under the same flow velocity, but the frequency remains stable at 4.15 Hz. This confirms the CS-TENG's durability and suitability as a long-term environmental monitoring sensor, mainly due to the use of silicone materials and the contact separation structure design.

The CS-TENG shows excellent potential as a sensing element for vortex flow velocity sensors, providing a novel sensing method. To investigate the shedding vortex sensing performance of the CS-TENG, the CS-TENG was positioned behind a blunt body with a diameter of 27 cm, and the incoming flow velocity was varied. The specific arrangement is shown in Figure S5b (Supporting Information).The optimal distance (L) between the blunt body and the sensor for matching theoretical and output frequencies is 7.5 cm and validated by the close match between theoretical and main frequencies of the output voltage signal at different distances, as shown in Figure 4h. With the optimal distance determined, the CS-TENG's sensing performance for blunt body shedding vortices at varying flow velocities was assessed. As the incoming flow velocity increases from 0.297 to 0.470 m s^{-1} (distance = 7.5 cm), the main frequency of the electrical signal increases linearly from 2.20 to 3.48 Hz, consistent with the shedding vortex frequency predicted by the Strouhal Number

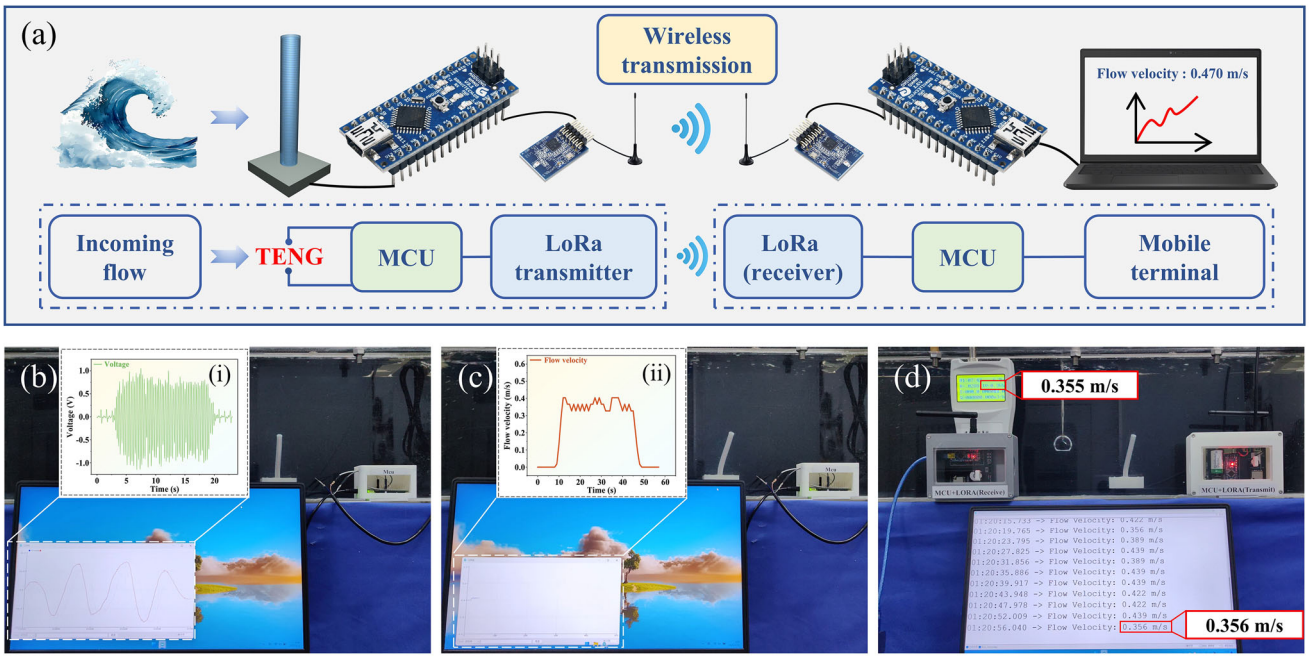

Figure 5. a) Workflow of the underwater flow monitoring system. b) Output signal collected by the MCU. c) Flow velocity output by the MCU. d) Comparison of CS-TENG and commercial velocity meter.

in Figure 4i. This demonstrates the CS-TENG's potential as a sensing element for vortex flow velocity sensors, offering a new sensing method.

2.3. The Demonstration of CS-TENG

Previous studies have demonstrated the potential of CS-TENG as an accurate sensor for measuring flow velocity. To enable its practical application, this work developed an underwater flow velocity monitoring system using CS-TENG, which achieves wireless real-time monitoring through by intergrating the MCU with the LoRa.

The system workflow involves signal collection, processing, calculation, and wireless transmission, as shown in **Figure** 5a. Specifically, the MCU first collects electrical signals from the CS-TENG, then processes them using a pre-programmed algorithm to determine real-time frequency. This frequency is input into an experimentally established flow velocity-frequency fitting equation to calculate real-time flow velocity. The MCU then transmits the result via LoRa, where a receiver interfaced with another MCU captures the data and relays it to a mobile terminal. Through this integrated process, the system successfully accomplishes wireless real-time monitoring of the flow velocity.

The output signal of CS-TENG recorded by the microcontroller and real-time flow velocity monitoring results are demonstrated in Figure 5b,c and Movies S1 and S2 (Supporting Information). A segment of the output signal data is stored locally to highlight waveform characteristics, as shown in Figure 5bi; meanwhile, a portion of the flow velocity results is stored locally to visualize dynamic changes over time, illustrated in Figure 5bii. These visualizations intuitively reflect the sensor's measurement stability and response characteristics. The underwater flow velocity monitoring system's performance is compared with a commercial flow velocity meter in Figure 5d and Movie S3 (Supporting Information), demonstrating that the CS-TENG exhibits comparable or superior accuracy in underwater applications.

3. Conclusion

In conclusion, this paper presents a flexible flow velocity sensor (CS-TENG) based on the contact-separation mode of TENG for real-time omnidirectional flow velocity monitoring. The CS-TENG features a core-sheath structure, where the outer sheath vibrates periodically due to the VIV effect. The sensor leverages VIV effect to facilitate the contact-separation between the outer sheath and inner core, and generates an electrical signal in response to the incoming flow excitation. Experimental results demonstrate a strong linear relationship between the main frequency of the electrical signal output from the CS-TENG and the flow velocity. By optimizing the structural parameters, the linear correlation coefficient between frequency and flow velocity reaches 0.992, with a start-up flow velocity of 0.297 m s^{-1}. The CS-TENG's tested velocity range (0.297–0.931 m s^{-1}) covers typical coastal and mid-ocean surface currents (0.1–1 m s^{-1}), with structural tunability enabling potential adaptation to broader marine environments. However, its performance at extreme velocities (>1 m s^{-1}) and depths, as well as long-term durability under corrosive conditions, remains unvalidated and requires further study. The CS-TENG exhibits a fast response time, capable of detecting changes in incoming flow velocity within 1.062 s. It features a fully enclosed structure and utilizes corrosion-resistant silicone material, ensuring its reliability and longevity in marine environments. To put the CS-TENG into practical application,

this paper designs an underwater flow velocity monitoring system based on the CS-TENG. The system utilizes the signal processing capabilities of MCU to locally process data, eliminating the need for a wired connection to a computer. Additionally, the LORA is employed to transmit monitoring results in real-time to a mobile terminal. This paper highlights the application potential and development prospects of the CS-TENG as a flow velocity sensor, offering a new viable solution for underwater flow velocity monitoring and contributing to the advancement of active sensor, sustainable sensing technologies in environmental energy harvesting.

4. Experimental Section

Fabrication of the CS-TENG: The flow velocity sensor (CS-TENG) designed in this paper consists of an outer sheath and an inner core. The outer sheath was made of flexible silicone material embedded with conductive yarn, and the inner core was a silicone rod wrapped with copper wires, as illustrated in Figure S1 (Supporting Information). The production process of the shell is as follows: First, two semicircular cavity molds (with radii of 7 and 9 mm) were designed using SolidWorks, and were 3D-printed. The molds were then assembled. Ecoflex00-20 silicone gel was prepared in a 1:1 ratio by weight, degassed in a vacuum chamber to remove air bubbles, and poured into the 7 mm molds. A 5 mm optical shaft was carefully inserted into the mold, and the assembly was placed in a drying oven at 48 °C to cure for 5–6 h. After curing, the solidified silicone was removed from the mold, and the conductive yarn was wound around the outer layer to form the inner layer of the outer sheath. The same silicone preparation process was repeated for the 9 mm mold. The inner layer was then carefully placed into the mold, and the curing process was repeated. The final product was a hollow sheath with an inner diameter of 5 mm and an outer diameter of 9 mm. The production process of the inner core is as follows: The inner core was made from a silicone rod, around which a 0.3 mm diameter copper wire was tightly wound. The outer sheath and inner core were then assembled onto the designed base. The upper end of the sensor was capped with a 5 mm diameter silicone rod, which was sealed with Kraft glue to complete the sensor.

Numerical Simulation of CS-TENG: COMSOL Multiphysics (Version 6.0) was used to establish a 2D axial cross-section model of the core-sheath structure. The sheath was fixed in the flow-parallel direction (displacement = 0 mm) while allowing free movement perpendicular to the flow. The Multiphysics used in this model was Fluid-Solid Interaction. The model locally encrypts the motion area of the sheath. Grid independence was verified by evaluating results with four mesh sizes: 8714, 13 780, 32 468, and 56 714 elements. The mesh with 32 468 elements was selected as it provided consistent results, confirming grid independence.

COMSOL Multiphysics (Version 6.0) was used to establish the potential distribution during the working process, with critical parameters reported as follows: the charge density was set as 3e–8 C m^{-2}, and the dielectric constants were specified as 3 for the silicone material and 1 for copper.

Circulating Flume: The flow velocity sensing performance of the CS-TENG was tested using a circulating flume. The flume was driven by a variable frequency submersible pump to generate water flow. The flow velocity (0–0.931 m s^{-1}) was controlled by adjusting the submersible pump's outlet flow velocity and head via a frequency converter. To ensure uniform and smooth water flow, four deflector plates and two sets of circular flow channels were used.

Output Performance Measurement of the CS-TENG: The electrical signals of CS-TENG were measured by an electrostatic meter (Keithley 6512), including open-circuit voltage, short-circuit current, and transferred charge. They were sent to the computer by a DAQ unit (NI-9215). Then these electrical signals were visualized and saved using LabVIEW software on the computer. After the submersible pump stabilized, signals output by the CS-TENG were collected. The sampling rate was set at 500 Hz, and data acquisition duration was 30 s under different working conditions. In the demo, the MCU model used for signal collection and processing was Arduino Nano, with the core being ATMEGA328P. The module employed for wireless transmission is LoRa Ra-02, and it communicates with the MCU through the SPI mode, and the frequency band of the wireless signal is 433 MHz.

Supporting Information

Supporting Information is available from the Wiley Online Library or from the author.

Acknowledgements

This research work was supported by the National Natural Science Foundation of China (52371345). The authors confirm that all figures, including the table of contents image, are original and created by the research team. No artificial intelligence tools were utilized in the production of this manuscript.

Conflict of Interest

The authors declare no conflict of interest.

Data Availability Statement

The data that support the findings of this study are available from the corresponding author upon reasonable request.

Keywords

flow velocity sensors, flexible sensors, triboelectric nanogenerators, vortex-induced vibration (VIV)

Received: April 1, 2025
Revised: June 4, 2025
Published online:

[1] H. van den Boom, J. Koning, P. Aalberts, in *Offshore Technol. Conference*, Offshore Technology Conference, **2005**.
[2] P. Wang, X. Tian, T. Peng, Y. Luo, *Ocean Eng.* **2018**, *147*, 148.
[3] D. Karanjai, S. Nallayarasu, S. K. Bhattacharya, *Experimental and Numerical Investigations on VIV Response of a Pipe in Shear Flow*, Vol. *8*, American Society Of Mechanical Engineers, **2020**.
[4] G. Liu, H. Li, Z. Qiu, D. Leng, Z. Li, W. Li, *Ocean Eng.* **2020**, *195*, 106704.
[5] Y. Komachi, S. Mazaheri, M. R. Tabeshpour, *J. Vibroeng.* **2018**, *20*, 152.
[6] H. Pezeshki, H. Adeli, D. Pavlou, S. C. Siriwardane, *Proc. Inst. Civ. Eng.-Marit. Eng.* **2023**, *176*, 89.
[7] A. R. Prabowo, T. Tuswan, R. Ridwan, *Appl. Sci.* **2021**, *11*, 3954.
[8] S. Ifedapo Abdullahi, M. Hadi Habaebi, N. Abd Malik, *Bull. Electr. Eng. Inform.* **2019**, *8*, 777.
[9] X. Li, X. Yao, C. Wang, L. Zhu, *J. Phys. Conf. Ser.* **2020**, *1584*, 12068.
[10] L. Ge, J. Chen, G. Tian, J. Ahmed, Q. Huang, Z. Hu, *Flow Meas. Instrum.* **2021**, *78*, 101882.
[11] S. Chen, Y. Wu, S. Liu, Y. Yang, X. Wan, X. Yang, K. Zhang, B. Wang, X. Yan, *J. Mar. Sci. Eng.* **2023**, *11*, 206.
[12] S. Catsamas, B. Shi, B. Deletic, M. Wang, D. T. McCarthy, *Sensors* **2022**, *22*, 7451.

[13] G. Shen, J. Ma, Y. Hu, J. Li, T. Cheng, J. Wen, *Sensors* **2022**, *22*, 4832.
[14] C. Ge, J. Ma, Y. Hu, J. Li, Y. Zhang, X. He, T. Cheng, J. Wen, *Adv. Mater. Technol.* **2023**, *8*, 2201296.
[15] A. Venugopal, A. Agrawal, S. V. Prabhu, *Sens. Actuators A Phys.* **2011**, *170*, 8.
[16] Z. L. Wang, J. Song, *Science* **2006**, *312*, 242.
[17] F.-R. Fan, Z.-Q. Tian, Z. L. Wang, *Nano Energy* **2012**, *1*, 328.
[18] C. Zhao, T. Du, B. Ge, Z. Xi, Z. Qian, Y. Wang, J. Wang, F. Dong, D. Shen, Z. Zhan, M. Xu, *Small* **2024**, *20*, 2307680.
[19] C. Zhao, D. Liu, Y. Wang, Z. Hu, Q. Zhang, Z. Zhang, H. Wang, T. Du, Y. Zou, H. Yuan, X. Pan, J. Mi, M. Xu, *Nano Energy* **2022**, *94*, 106926.
[20] M. Esteban, D. Leary, *Appl. Energy* **2012**, *90*, 128.
[21] C. Zhu, M. Wu, C. Liu, C. Xiang, R. Xu, H. Yang, Z. Wang, Z. Wang, P. Xu, F. Xing, H. Wang, M. Xu, *Adv. Energy Mater.* **2023**, *13*, 2301665.
[22] H. Yu, Z. Xi, H. Du, H. Yang, Z. Qian, X. Guo, Y. Guo, Y. Huang, T. Du, M. Xu, *Adv. Energy Mater.* **2024**, *14*, 202400585.
[23] J. Liu, P. Xu, J. Zheng, X. Liu, X. Wang, S. Wang, T. Guan, G. Xie, M. Xu, *Nano Energy* **2022**, *101*, 107633.
[24] X. Wang, C. Zhu, M. Wu, J. Zhang, P. Chen, H. Chen, C. Jia, X. Liang, M. Xu, *Sens. Actuators A Phys.* **2022**, *344*, 113727.
[25] Y. Zou, M. Sun, X. Zhang, J. Wang, F. Li, F. Dong, Z. Zhao, T. Du, Y. Ji, P. Sun, M. Xu, A Flexible, *Small* **2024**, *20*, 202309759.
[26] Y. Zou, M. Sun, S. Li, X. Zhang, L. Feng, Y. Wang, T. Du, Y. Ji, P. Sun, M. Xu, *Nano Energy* **2024**, *122*, 109316.
[27] T. Du, Z. Chen, F. Dong, H. Cai, Y. Zou, Y. Zhang, P. Sun, M. Xu, *Adv. Funct. Mater.* **2024**, *34*, 202313794.
[28] C. Wu, A. C. Wang, W. Ding, H. Guo, Z. L. Wang, *Adv. Energy Mater.* **2019**, *9*, 201802906.
[29] M. Wu, C. Zhu, X. Liu, H. Wang, J. Si, M. Xu, J. Mi, *Mater. Today Energy* **2024**, *41*, 101529.
[30] M. Wu, C. Zhu, J. Si, H. Wang, M. Xu, J. Mi, *Adv. Mater. Technol.* **2023**, *8*, 202300919.
[31] M. Mousavi, M. Alzgool, B. Davaji, S. Towfighian, *Small* **2024**, *20*, 1.
[32] M. Alzgool, Y. Tian, B. Davaji, S. Towfighian, *Nano Energy* **2023**, *109*, 108282.
[33] X. Fu, S. Xu, Y. Gao, X. Zhang, G. Liu, H. Zhou, Y. Lv, C. Zhang, Z. L. Wang, *ACS Energy Lett.* **2021**, *6*, 2343.
[34] Y. Wang, E. Yang, T. Chen, J. Wang, Z. Hu, J. Mi, X. Pan, M. Xu, *Nano Energy* **2020**, *78*, 105279.
[35] W. Li, L. Lu, X. Fu, C. Zhang, K. Loos, Y. Pei, *ACS Appl. Mater. Interfaces* **2022**, *14*, 51018.
[36] Z. Deng, L. Xu, H. Qin, X. Li, J. Duan, B. Hou, Z. L. Wang, *Adv. Mater.* **2022**, *34*, 202205064.
[37] P. Cheng, M. Sun, C. Zhang, H. Guo, J. Shi, Y. Zhang, Y. Liu, J. Wang, Z. Wen, X. Sun, *IEEE Trans. Nanotechnol.* **2020**, *19*, 230.
[38] Y. Wang, Z. Qian, C. Zhao, Y. Wang, K. Jiang, J. Wang, Z. Meng, F. Li, C. Zhu, P. Chen, H. Wang, M. Xu, *Adv. Mater. Technol.* **2023**, *8*, 202201245.
[39] Q. Zhang, L. Li, T. Wang, Y. Jiang, Y. Tian, T. Jin, T. Yue, C. Lee, *Nano Energy* **2021**, *90*, 106501.
[40] S. He, Z. Wang, X. Zhang, Z. Yuan, Y. Sun, T. Cheng, Z. L. Wang, *ACS Appl. Mater. Interfaces* **2022**, *14*, 2825.
[41] M. Xu, Y.-C. Wang, S. L. Zhang, W. Ding, J. Cheng, X. He, P. Zhang, Z. Wang, X. Pan, Z. L. Wang, *Extrem. Mech. Lett.* **2017**, *15*, 122.
[42] Y. Yang, G. Zhu, H. Zhang, J. Chen, X. Zhong, Z.-H. Lin, Y. Su, P. Bai, X. Wen, Z. L. Wang, *ACS Nano* **2013**, *7*, 9461.
[43] Y. Xi, H. Guo, Y. Zi, X. Li, J. Wang, J. Deng, S. Li, C. Hu, X. Cao, Z. L. Wang, *Adv. Energy Mater.* **2017**, *7*, 1602397.
[44] P. Wang, L. Pan, J. Wang, M. Xu, G. Dai, H. Zou, K. Dong, Z. L. Wang, *ACS Nano* **2018**, *12*, 9433.
[45] Y. Qiao, W. Chang, A. J. Cheng, J. Wang, H. Zhang, Z. Sha, S. He, J. Zhang, S. Peng, C. H. Wang, *Nano Energy* **2023**, *118*, 109021.
[46] R. Violette, E. de Langre, J. Szydlowski, *Comput. Struct.* **2007**, *85*, 1134.
[47] R. Govardhan, C. H. K. Williamson, *J. Fluid Mech.* **2000**, *420*, 85.
[48] S. Krenk, S. R. K. Nielsen, *J. Eng. Mech.* **1999**, *125*, 263.
[49] S. Niu, S. Wang, L. Lin, Y. Liu, Y. S. Zhou, Y. Hu, Z. L. Wang, *Energy Environ. Sci.* **2013**, *6*, 3576.